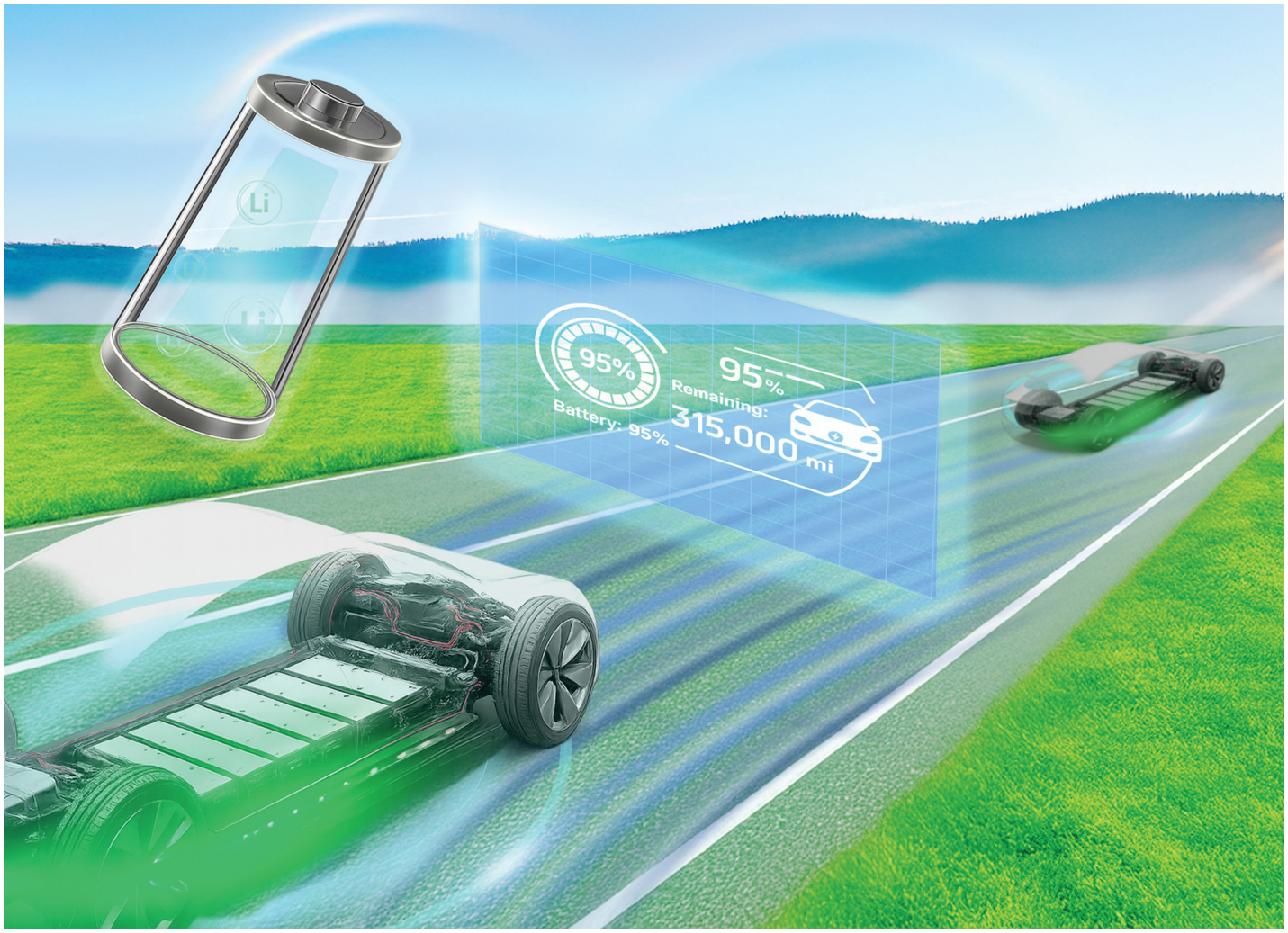

Showcasing research from Professor Daniel Brandell's team at the Ångström Advanced Battery Centre, Uppsala University, Uppsala, Sweden.

Uncovering the impact of battery design parameters on health and lifetime using short charging segments

A machine learning framework, coupled with a physics-based digital twin model, connects battery design and manufacturing choices to real performance under different charging and operating conditions. By analysing short charging segments from fast-charging scenarios, the software identifies critical design factors such as ionic diffusion, electrode thickness, particle size, ion concentration, and porosity. These are integrated with interpretable usage signals—voltage, current, and capacity patterns—to enhance prediction reliability of the battery, offering a bridge between physical behaviour and data-driven insights.

Image reproduced by permission of Wendi Guo from *Energy Environ. Sci.*, 2025, **18**, 8462.

As featured in:

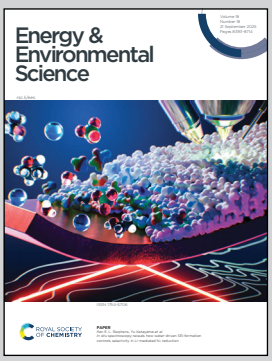

See Wendi Guo, Daniel Brandell *et al.*, *Energy Environ. Sci.*, 2025, **18**, 8462.

ROYAL SOCIETY OF CHEMISTRY

rsc.li/ees

Registered charity number: 207890

Energy & Environmental Science

ROYAL SOCIETY OF CHEMISTRY

PAPER

View Article Online
View Journal | View Issue

Cite this: *Energy Environ. Sci.*, 2025, **18**, 8462

Uncovering the impact of battery design parameters on health and lifetime using short charging segments

Wendi Guo, *[a] Søren Byg Vilsen, [b] Yaqi Li, [c] Ashima Verma, [a] Daniel Ioan Stroe [c] and Daniel Brandell *[a]

Frequent fast charging of lithium-ion batteries (LiBs) demands robust health monitoring, not only to ensure long-term performance and user confidence, but also to support emerging applications such as vehicle-to-grid (V2G), where energy flows bidirectionally between EVs and the grid. Without clear insight into how upstream design parameters such as solid-state diffusion coefficient, electrode thickness, particle radius, lithium-ion concentration, and porosity impact battery health in real-world use, however, valuable opportunities to optimize early-stage designs and develop tailored usage strategies to mitigate degradation may be lost. This work proposes a machine learning (ML) framework built on a digital twin model that links key design parameters to real-world behaviors of graphite/nickel–manganese–cobalt–oxide LiBs under a diverse range of fast charging protocols, depths of discharge, and dynamic discharge profiles representative of applications in Nordic climates. The framework infers six key design parameters directly from short charging segments, enabling rapid health prediction within seconds. Notably, this approach improves the robustness of health and lifetime predictions by up to 65% and 69%, respectively, compared to baseline multi-layer perceptron and linear regression models, while also outperforming the baseline random forest model, with a training time of 1 second. The strong physical correlation between capacity variability and three design parameters—solid-state diffusion coefficient, particle radius, and electrode thickness—during fast charging highlights their vital role in determining the degradation pathways. The framework can be readily integrated into upstream workflows and battery management systems, enabling end users to tailor usage patterns and guiding developers toward improved design strategies.

Received 11th June 2025,
Accepted 11th August 2025

DOI: 10.1039/d5ee03268g

rsc.li/ees

Broader context

Batteries are the heart of the future energy systems, enabling electric transportation and the integration of renewables into the electricity grid. Their critical role underscores the urgency of advancing battery technologies. A battery's design fundamentally shapes its performance and lifetime. Connecting design parameters to long-term behavior is key to advancing durable lithium-ion batteries for broad electrification needs. In this work, we present a machine learning framework combined with a digital twin model to uncover sensitive design parameters from short charging segments. By integrating manually engineered, interpretable features, the framework improves both health and lifetime prediction. Through this framework, design parameters such as electrode thickness, porosity, lithium-ion concentration, and ionic diffusion coefficient can be inferred and tracked as they evolve under specific operating conditions, enhancing both the accuracy and robustness of performance predictions. We demonstrate that battery design plays a primary role in predicting aging behavior. Overall, this work establishes an effective link between design and real-world applications, ultimately accelerating the development of safer and longer-lasting next-generation batteries.

1. Introduction

Fast charging is not only essential for accelerating battery electric vehicles (BEVs) adoption, but also plays a critical role in unlocking the full potential of batteries – improving user experience, enabling the development of real-time optimization strategies, and supporting emerging energy services such as vehicle-to-grid (V2G), where frequent, rapid energy exchange

[a] *Department of Chemistry – Ångström Laboratory, Uppsala University, Lägerhyddsvägen 1, Uppsala 75121, Sweden. E-mail: wendi.guo@kemi.uu.se, daniel.brandell@kemi.uu.se*
[b] *Department of Mathematical Sciences, Aalborg University, Skjernvej 4, Bygning: A, Aalborg 9220, Denmark*
[c] *Department of Energy, Aalborg University, Pontoppidanstræde 101, Aalborg 9220, Denmark*

between BEVs and the grid imposes additional demands on performance, longevity, and resilience. To ensure safety in BEVs[1] and stable operation of energy storage systems,[2] especially under fast charging, timely and accurate evaluation of battery health metrics such as capacity[3] and remaining useful life (RUL)[4] is crucial. Without understanding how electrode-specific design factors influence health status under real-world fast charging conditions, valuable insights may be lost. These insights are critical for informing early design improvements of next-generation batteries and optimizing usage strategies to reduce degradation.[5] Due to the complexity of multiscale physical and chemical processes, this remains a significant challenge, particularly when incorporating electrode-level design factors under realistic operating conditions.[6] Moreover, despite a growing interest, studies replicating real-world EV usage remain scarce in literature, as battery discharging is often conducted under constant current (CC)[1] conditions. Closing this gap between laboratory aging tests and realistic usage patterns is crucial to advancing the practical performance of EVs.[7]

A surge of modelling efforts has recently focused on predicting LiBs state-of-health (SOH) and lifetime, including physics-based,[8–10] data-driven,[11–13] and hybrid methods.[14–17] These methods often rely on extracting key features[4,18,19] from cycling data – either collected during duty cycles[20] or generated through physics-based models.[21,22] Commonly used features include raw measurements such as (current, voltage),[3,23] temperature,[24] and impedance,[25] as well as processed diagnostic indicators like incremental capacity (IC)[26] and differential voltage (DV)[27] analysis,[28] electrochemical impedance spectroscopy (EIS)[29,30] and time-series trend of specific metrics.[31] While data-driven methods have shown strong feasibility in predicting battery health, they often rely heavily on high-quality sensing data[32] and offer limited interpretability of the underlying physical mechanisms. As a result, critical early-stage design factors, such as geometrical properties of the electrodes and intrinsic material properties (*e.g.*, diffusivities, maximum lithium concentration, *etc.*), often remain unidentified. In contrast to data-driven models, physics-based models are built on multiphysics coupling equations[33] that describe the internal electrochemical behavior of batteries.[34] These models offer valuable insights into the link between the physics and chemistry of the electrode and performance parameters such as capacity, energy, resistance, and electrochemical responses.[35,36] However, they often lack flexibility needed to adapt to diverse operational scenarios – such as V2G applications, where data exchange between EVs and charging infrastructure is required. This limits their practicality for health diagnostics and design-related insights in real-world settings. Thus, a clear gap remains in establishing a design-to-performance mapping that not only yields more comprehensive and quantitatively precise insights than physics-based or data-driven approaches alone, but also directly links battery design decisions to real-world deployment outcomes.

To balance the need for accurate health status prediction with efficient identification of key cell design parameters, models are being developed that incorporate insights from aging mechanisms for battery lifetime prognostics.[15,37] Aging in LiBs is typically categorized into three main modes,[38] *i.e.*, loss of active material in the positive electrode (LAM_{PE}), in the negative electrode (LAM_{NE}), and loss of lithium inventory (LLI). These can be quantified using techniques such as impedance spectroscopy,[39] acoustic spectroscopy,[40] and X-ray tomography.[41] Additional insights come from post-mortem analysis – such as scanning electron microscope (SEM),[42] Raman spectroscopy, and X-ray photoelectron spectroscopy (XPS)[43] – or from different types of *in situ* measurements.[44] However, these methods are often costly and unsuitable for real-time monitoring during battery operation. To enable faster, non-invasive and non-destructive identification of aging mechanisms, recent efforts focus on analyzing physically meaningful indicators derived from battery data, including half-cell open-circuit voltage (OCV) curves,[45] lithium plating potential,[46] and shifts in IC peak positions or areas.[47,48] It is now well known that aging behavior in LiBs is fundamentally influenced by intrinsic design parameters[49] such as electrode thickness,[50] particle size,[51] and ionic diffusivity[52]—factors that are difficult to study directly under real-world operating conditions. The interaction between these design parameters and the battery usage patterns plays a critical role in shaping the dynamic of battery aging. Even with the same active materials, cells can exhibit highly different aging patterns due to differences in structure and usage scenarios.[49] This divergence becomes more pronounced during fast charging, where high C-rates lead to sluggish mass transport.[53] Bridging the gap between observable performance and upstream design parameters requires a predictive framework that captures variations in electrode design parameters and operating conditions, accelerating the discovery of next-generation batteries and promoting a more sustainable energy future. Despite growing interest in aging mode identification, the impact of these sensitive design parameters on long-term battery behavior remains largely unexplored.

To address the challenge of linking design parameters with real-world battery behavior, we propose a machine learning (ML) framework that maps partial charging segments to cell design parameters derived from a digital twin (DT) model.[10] These physically grounded parameters, such as solid-state diffusion coefficient, electrode thickness, particle radius, lithium-ion concentration, and porosity, are integrated to improve health and lifetime prediction under fast-charging conditions. We develop this framework using graphite/$LiNi_{0.5}Mn_{0.3}Co_{0.2}O_2$ (NMC532) LiB cells, tested across a range of C-rates (1C to 2C) and two multistep fast-charging protocols. To simulate realistic EVs operation, dynamic discharging profiles covering 70% to 100% depth of discharge (DOD) were applied at four ambient temperatures representative of Nordic climates. Previous work has employed DT-assisted diagnostics to identify aging mechanisms and modes in these cells.[54] In this study, we infer six design parameters – five sensitive parameters identified in a previous study,[10] plus the solid-state diffusion coefficient – directly from short charging curves, enabling efficient extraction of design-related features with minimal computational cost. These inferred parameters then serve as physically interpretable inputs that enhance the performance of both SOH estimation and RUL

prediction. Notably, the proposed battery-design-aware ML framework can achieve early-life prediction, with the error stabilizing after just 80 equivalent full cycles (EFCs) – corresponding to 8.4% of the median cycle life – and comparable to the 100-cycle benchmark used in Severson *et al.*[4] We find that design-related factors such as the negative electrode's diffusion coefficient, thickness, and particle size provide superior individual predictive strength for RUL prediction, demonstrating both high accuracy and stability. This partial charging approach offers practical value across a broad range of real-world applications with limited data availability, including emerging V2G, where frequent bidirectional energy exchange limits access to full charging curves. Our findings reveal, for the first time, that key battery design parameters can be uncovered from externally accessible signals, enabling more stable and interpretable predictions, offering a scalable and production-ready solution without requiring advanced sensor integration[18] into manufacturing lines.

2. Methods

2.1. Learning design parameters from partial charging segments

Our aim is to combine physics-based insights with data-driven models to fully leverage the potential of ML in battery diagnostics. The objective is not only to improve prediction accuracy but also to establish a link between battery modeling and understanding of the cell-specific design, all while minimizing design development effort. By selecting health indicators capture a wide range of aging behaviors-including hard-to-measure design parameters-we aim to evaluate whether incorporating these sensitive features can enhance prediction accuracy. However, integrating sensitive design parameters into predictive models presents three key challenges: (1) high experimental costs: measuring these parameters is both time-consuming and expensive,[55] especially in industrial contexts[56] of full-scale EV batteries. (2) Computational demands: running electrochemical simulations that incorporate multiple aging mechanisms over thousands of cycles requires substantial computational resources.[46] (3) Limited generalizability: without validation across diverse battery chemistries and usage conditions, the resulting datasets may lack robustness, reducing the reliability of ML surrogate predictions in real-world applications.

To address these challenges, we propose a battery-design-aware ML using a validated DT model. This framework can support health-informed decision-making across a range of applications, for example, assessing battery eligibility for grid connection in V2G scenarios. Instead of relying on extensive experiments or full-cycle simulations, we conduct a sensitivity sweep of key design parameters (Table S2). By simulating 1C CCCV charge–discharge cycles with variations in these parameters, we efficiently generate a wide range of charge–discharge curves (Fig. S6), along with corresponding voltage, SOC, cycle time, and their variations in time. Each parameter is sampled from a normal distribution within 1% relative standard deviation.[57] Fig. 1 illustrates our data processing pipeline. It starts with collecting.txt output files from COMSOL Multiphysics 6.3 simulations. We calculate SOC as the accumulated capacity Q and capacity change ΔQ using the following equation:

$$Q(t) = Q_0 \times \mathrm{SOC}(t)$$

$$\Delta Q(t) = Q(t) - Q_0$$

where $\mathrm{SOC}(t)$ represents the battery's SOC over time, Q_0 is the nominal capacity, and $\Delta Q(t)$ denotes the capacity variation. Next, we select partial charging segments (red rectangle in Fig. 1) and compute health indicators, which are described in detail below. Using the established mapping between voltage curves and design parameters, these parameters can be predicted from partial charging segments during real-time operation.

2.2. Synthetic battery health indicators with mechanism interpretation

This study utilizes fast-charging datasets published in previous research,[54,58] based on 18 650 cylindrical graphite/NMC532 cells with a nominal capacity of 2 Ah. Charging was performed using both constant current (CC) and multistep protocols at 1C, 1.3C, and 2C, ending with constant voltage (CV) until the current reached 0.01 A (C/20). Discharging followed the world harmonized light vehicles test cycle (WLTC) profile, constrained between 2.5 V (100%DOD) and 3.6 V (70%DOD). Cell lifetimes ranged from 110 to 972 equivalent full cycles (EFCs), with reference performance tests (RPTs) conducted every 100 EFCs, similar to periodic maintenance checks. These limited RPT data serve as training labels, with additional pseudo-labels generated *via* linear interpolation.[59] To account for varying voltage windows across tests, EFCs are computed by dividing the total discharged capacity by the nominal pre-cycling capacity (2 Ah). This normalization enables fair comparison across protocols and aligns better with real-world EV mileage than simple cycle counts.[55] More details are in Table S3 and Fig. S3 and S4. Only the two cells tested at 1.3C and 15 °C share identical conditions; all other factors, including charging/discharging protocols and temperatures, differ. To the best of our knowledge, this is the first dataset combining multiple fast charging protocols with dynamic discharging profiles across varying temperatures, specifically designed to reflect different user patterns.

Specifically, the maximum observed difference in lifetime across fast-charging conditions is 862EFCs-exceeding the average and minimum lifetimes by 127% and 782%, respectively. To investigate this divergence further, we apply manual feature engineering aimed at capturing a broad range of aging-related behaviors. Rather than refining specific features, we focus on selecting health indicators that reflect time dynamics, capacity trends, voltage and current patterns, and non-invasive IC/DV characteristics. While some of these may include effects unrelated to aging (Fig. 2(a)), they are intentionally preserved to reflect real-world sensor biases and enable fair comparison. This analysis ensures the physical interpretability of manually engineered features and serves as a baseline to assess whether design parameters extracted from random partial charging

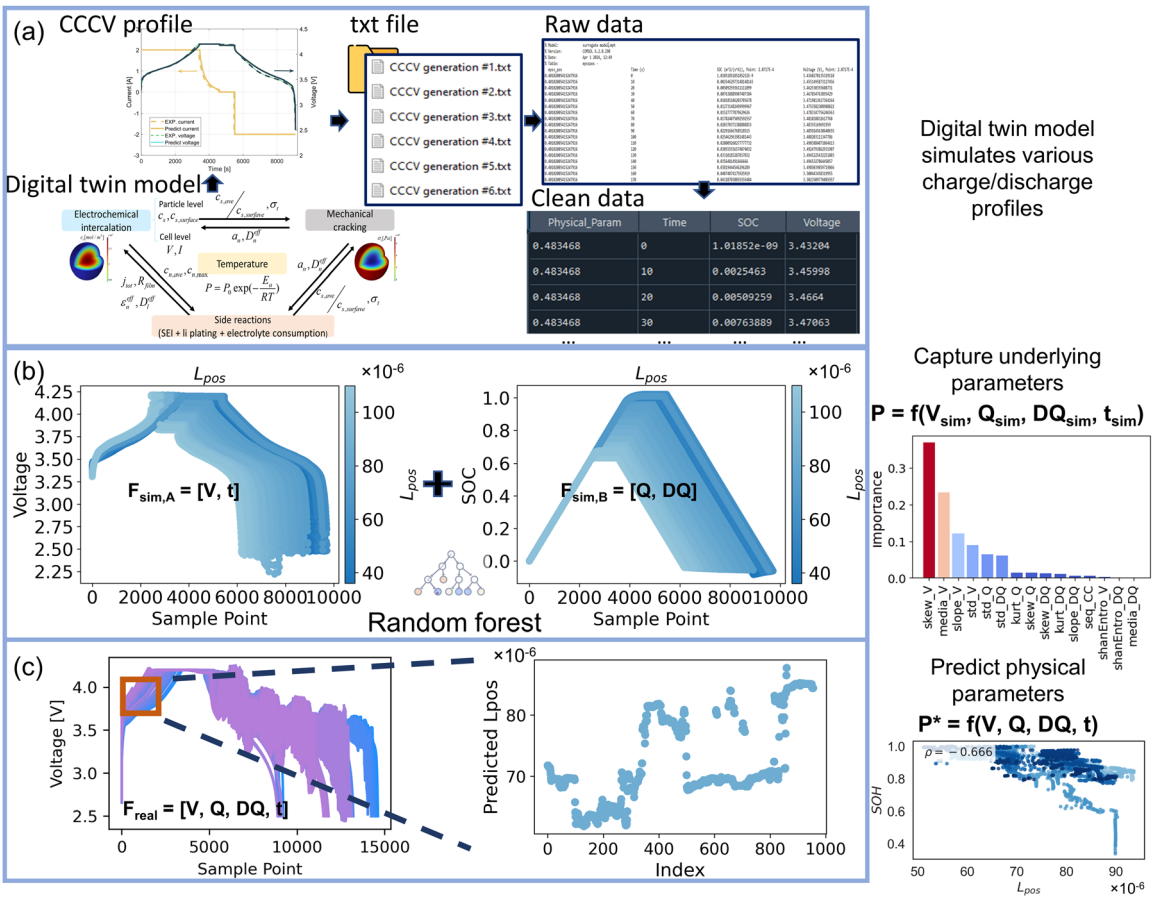

Fig. 1 Flowchart of learning design parameters from partial charging segments. (a) The DT model sweeps all sensitive design parameters to generate diverse charge/discharge profiles. (b) Illustration of selected data for design feature (*e.g.* positive electrode's thickness) mapping. Features are extracted from partial charging segments across four categories: voltage, time, capacity, and capacity variation (converted from SOC). These features serve as inputs to a random forest (RF) model for predicting design parameters. As an example, the right subplot displays the feature importance ranking for positive electrode's thickness L_{pos}. (c) Predicted design parameters are obtained from dynamic aging profiles in real-world applications. The right subplot shows one case of the correlation between L_{pos} and SOH, where function $f(\cdot)$ maps the four feature categories to design parameters that carrying insights into battery aging.

segments can more effectively capture aging behavior – ultimately enhancing health status prediction under unseen operating conditions. Sixteen features are selected, including charging time (Fig. 2(a)), end of charge voltage (EOCV) (Fig. 2(b)), IC peak shift and shrink (Fig. 2(c)), and DV valley shift and shrink (Fig. 2(d)), which strongly correlate with LLI and LAM54 (see Fig. S5). Additional features include geometric curves of voltage (V) (Fig. 2(e)), capacity deviation (ΔQ) (Fig. 2(f)), and current (I) (Fig. 2(g)), along with statistical metrics from V–Q (Fig. 2(e)), ΔQ (Fig. 2(f)), and I (Fig. 2(g)) sequence, such as median, standard deviation (std), kurtosis (kurt), skewness (skew), and shannon entropy (ShanEn). A detailed explanation is provided in Table S1. Fig. S1 presents the evolution of feature values under different operational conditions.

2.3. Proposed physics informed health prediction

Traditional ML methods for health status prediction struggle with feature divergence. Their adaptability drops when training and testing datasets are split randomly, leading to poor performance under unseen conditions. This limitation stems from the heterogeneous distribution of battery aging behaviors (see Fig. S3). One approach to correcting this feature divergence is domain adaptation, such as MMD[60] and CORAL,[24] tested with a RF model (see Fig. S7 and SI2). Furthermore, we also explore a simpler approach called 'mixed inputs',[59] which concatenates charging protocols and temperature information as [C1, C2, C3, C4, T] after feature selection. A Monte Carlo experiment with 100 simulations was performed across the entire sample space. Fig. S7 compares the prediction performance of five models: baseline RF (with default hyperparameters), MMD-aided RF, CORAL-aided RF, MMD-aided RF with mixed-input aging indicators, and CORAL-aided RF with mixed-input aging indicators. Results indicate that the MMD-aided RF consistently provides better alignment with ground truth, particularly for cells with exceptionally short or long lifetimes. This model serves as the pure ML baseline for the comparisons in Section 3.1.

We propose an ML framework to extract and incorporate sensitive design parameters. The feature vector $F = \mathrm{HI}_s$ [V_s, Q_s, DQ_s] (detailed in Table S1) is derived from the DT model, where voltage, current, and SOC are sampled every 10 s over a 9300 s

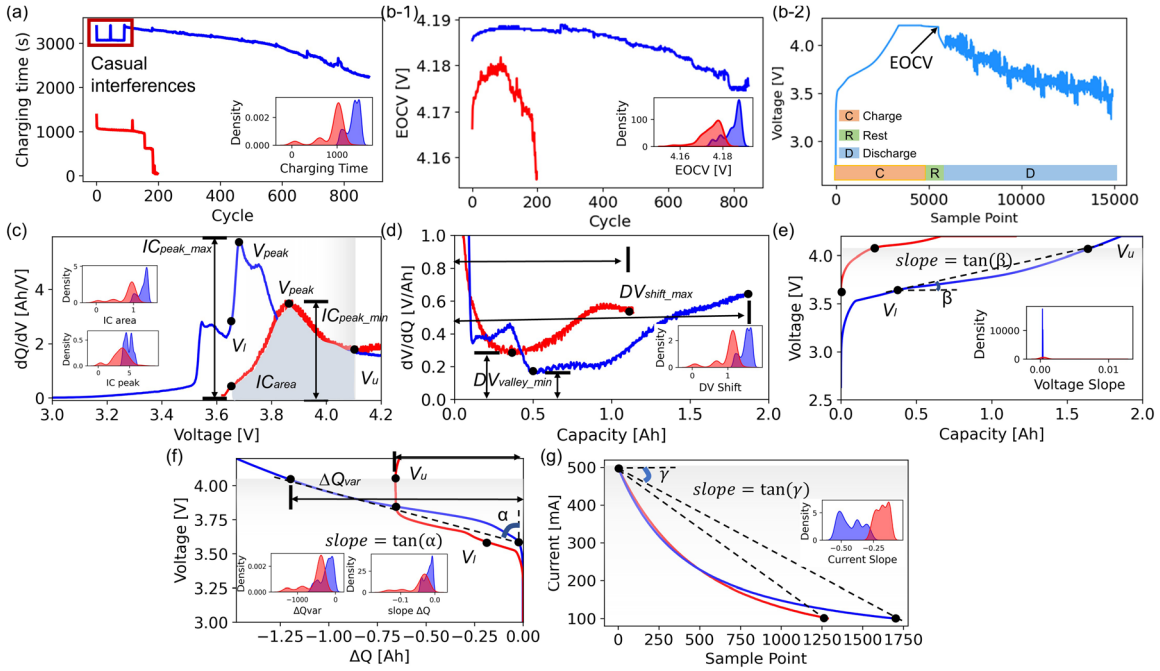

Fig. 2 Feature extraction and divergence distribution between two aging conditions at 1C, 25 °C (blue) and 2C, 0 °C (red): (a) charging time, (b-1) end-of-charge voltage (EOCV), (b-2) schematic illustration of EOCV data collecting during charging–discharging cycles, (c) IC curve shift (d) DV curve shift; geometry pattern of (e) voltage, (f) capacity deviation, and (g) current. V_l and V_u indicate the charging range within which features are extracted.

interval (Fig. S6). These extracted features are then used to train the ML framework outlined in Fig. 3, which consists of two sub-models. Sub-model 1 takes the feature vector F as input and predicts the label P, comprising six key design parameters from the DT: [L_{neg}, $r_{p,neg}$, D_{neg}, L_{pos}, $C_{p,max}$, ε_{pos}]. It generates the predicted P_1 based on random charging segments. Next, sub-model 2 uses the feature vector F and the predicted design parameters P_1 to estimate SOH (based on capacity fade) and predict RUL. In real-world applications such as V2G, the trained model can operate on short charging segments to simultaneously predict SOH and RUL under varying driving and operating conditions (Fig. S17), based on labels obtained from periodic maintenance checks. To apply the model to other battery systems, hyperparameter fine-tuning is required.

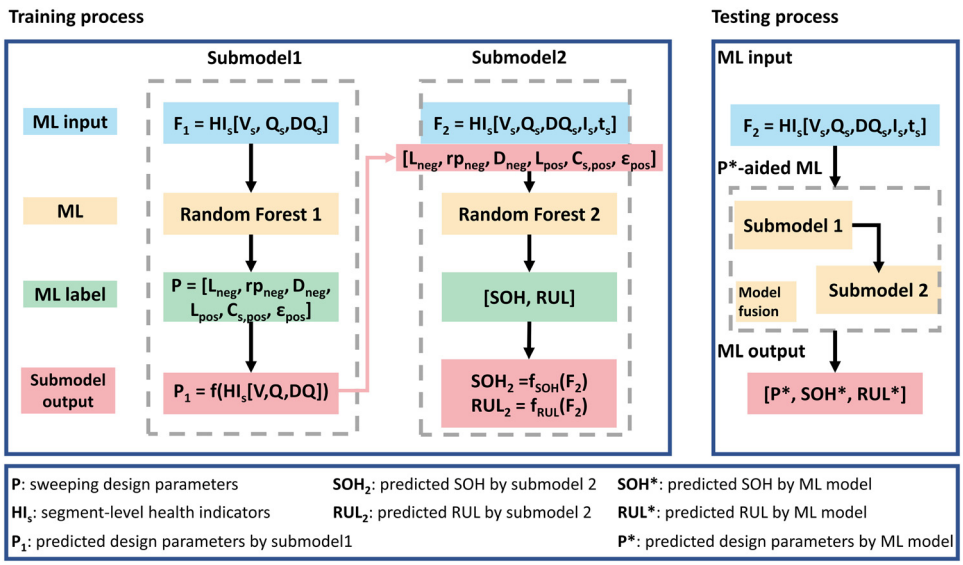

Fig. 3 Flowchart of the proposed ML pipeline for battery health status prediction. The framework includes two sub-models that integrate design parameters obtained from a DT model. Sub-model 1 takes the extracted feature vector F as input and predicts six design parameters: [L_{neg}, $r_{p,neg}$, D_{neg}, L_{pos}, $C_{s,max}$, ε_{pos}]. Sub-model 2 uses F and the predicted design parameters to estimate SOH (based on capacity fade) and RUL. During testing, features from short-term charging segments (subscript s) are used to provide real-time SOH estimation and RUL prediction.

This can be performed using the training set with K-fold cross-validation. These aspects will be explored in future work.

To evaluate the proposed ML model, the dataset was split into training and testing sets based on distinct combinations of temperature, charging protocol, and driving profile (Fig. S17). Feature vectors F were randomly assigned across these splits to assess the model's ability to generalize to unseen conditions. Model accuracy was then evaluated across three cases to analyze the effect of integrating design parameters on SOH estimation and RUL prediction performance.

3. Results and discussion

3.1. Performance including learned design parameters

The validation results of the proposed ML pipeline with or without six design parameters (P^*) are shown in Fig. 4. Fig. 4(a) presents the errors of estimated SOH, SOH* and predicted RUL, RUL*, using features extracted from [3.65 V, 4.1 V].[59] Using randomly train-test dataset split (data from cell 1–10), the data ratio for training is 0.8, leaving 0.2 for the test set. It can be seen from Fig. 4(a-1) that with P^*, most estimated SOH* errors are below 0.02 and predicted RUL* errors are below 100 EFCs, with predictions tightly clustered around the ground truth. In contrast, without P^* (Fig. 4(a-2)), the SOH* error distribution is broader and shows significant deviation, particularly at low SOH ranges (<0.9). The RUL* predictions tend to be overestimated during the early aging stages, resulting in larger deviations, with many absolute errors exceeding 200 EFCs. The cumulative distribution function (CDF) for estimated SOH* and predicted RUL* errors is given in Fig. 4(b). For SOH estimation (Fig. 4(b-1)), the CDF shows that over 95% of predictions with P^* can achieve errors below 3.5%, compared to only $\sim$80% without P^*. The boxplot further confirms this improvement, with a lower median error and tighter interquartile range, indicating both higher accuracy and reduced variance when P^* is integrated. For RUL prediction (Fig. 4(b-2)), at a 30% error rate threshold, the model with P^* reaches 85% probability, compared to just 75% without P^*. The median RUL error drops from 16% (without P^*) to 12% (with P^*), and the narrower interquartile range further reflects enhanced prediction stability. These results highlight that embedding P^* features consistently improves both accuracy and reliability-especially for long-term aging prediction under varying charging protocols and dynamic discharging profiles.

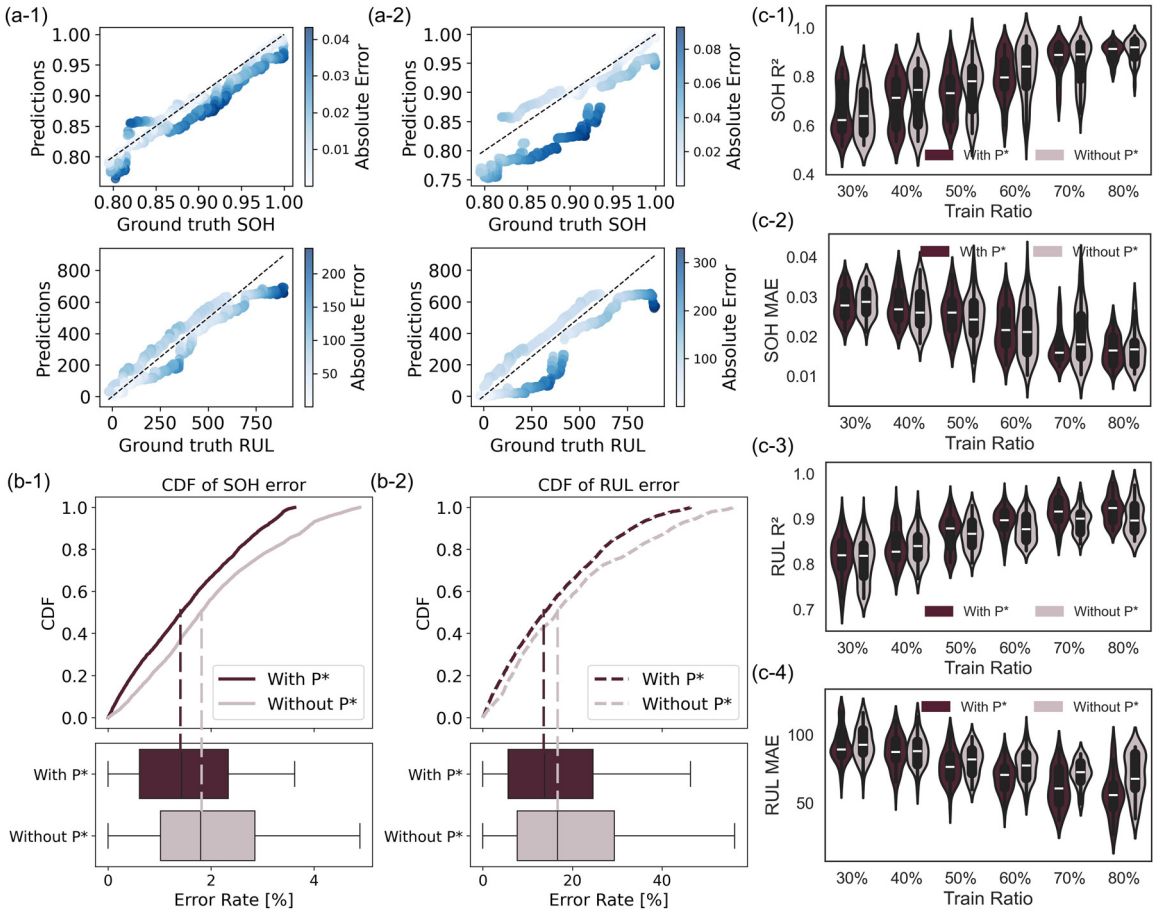

Fig. 4 Performance evaluation of the proposed ML pipeline with or without all six P^*. (a) Parity plots for the RF model for one random train-test split (80% training, 20% testing): (a-1) with P^* and (a-2) without P^*. (b) Cumulative error distributions comparing predictions with and without P^* for both (b-1) SOH and (b-2) RUL. (c) Monte Carlo simulations of model with 100 random seeds, using varying train-test ratios, with and without P^*.

To ensure the robustness of P^*-aided ML battery health prognostics, the training dataset ratios range from 30% to 80%, and the violin figures (Fig. 4c) are obtained by performing 100 Monte Carlo simulations to select the training cells. The better performances with P^* are reflected by lower errors (MAE) and higher fitting coefficients (R^2). Fig. 4(c-1) and (c-2) compares SOH estimation performance using both R^2 and MAE across different training data ratios. At 30%, the model without P^* shows a slightly higher median R^2 (0.63 *vs.* 0.61), while the model with P^* yields a lower median MAE (0.027 *vs.* 0.029), indicating better precision under limited data. From 40% to 60%, the without P^* model achieves higher median R^2 (0.71–0.84), but greater variability. In contrast, the P^*-aided model maintains narrower R^2 and MAE distribution, suggesting improved robustness. At 70%, R^2 is marginally higher without P^* (0.90 *vs.* 0.88), but the model with P^* achieves a lower median MAE (0.015 *vs.* 0.017). At 80%, both models achieve similar high R^2 (0.92), yet the P^*-aided model displays reduced MAE variance, reinforcing its stability. In summary, while the pure ML model may offer higher median R^2 at 40–60% training ratios, integrating P^* consistently reduces prediction spread, and at higher training ratios (70–80%) achieves superior accuracy and reliability, which is critical for real-world deployment. Fig. 4(c-3) and (c-4) presents the performance of RUL prediction in terms of R^2 and MAE, comparing models with and without P^* features. At a 30% training ratio, the model with P^* achieves a slightly higher median R^2 (0.83 *vs.* 0.82) and lower MAE (89 *vs.* 93), indicating better performance under limited data. At 40%, R^2 is marginally higher without P^* (0.84 *vs.* 0.82), but the model with P^* still shows a lower MAE (88 *vs.* 90). From 50% to 70%, the inclusion of P^* consistently improves both R^2 (0.88–0.92) and MAE (0.015–0.025), confirming its contribution to both the fit quality and predictive accuracy-even if variance is not always reduced. At 80%, the benefit of P^* becomes even more pronounced, with P^* achieving higher R^2 (0.92 *vs.* 0.87) and lower MAE (56 *vs.* 66), reflecting both superior accuracy and robustness. Overall,

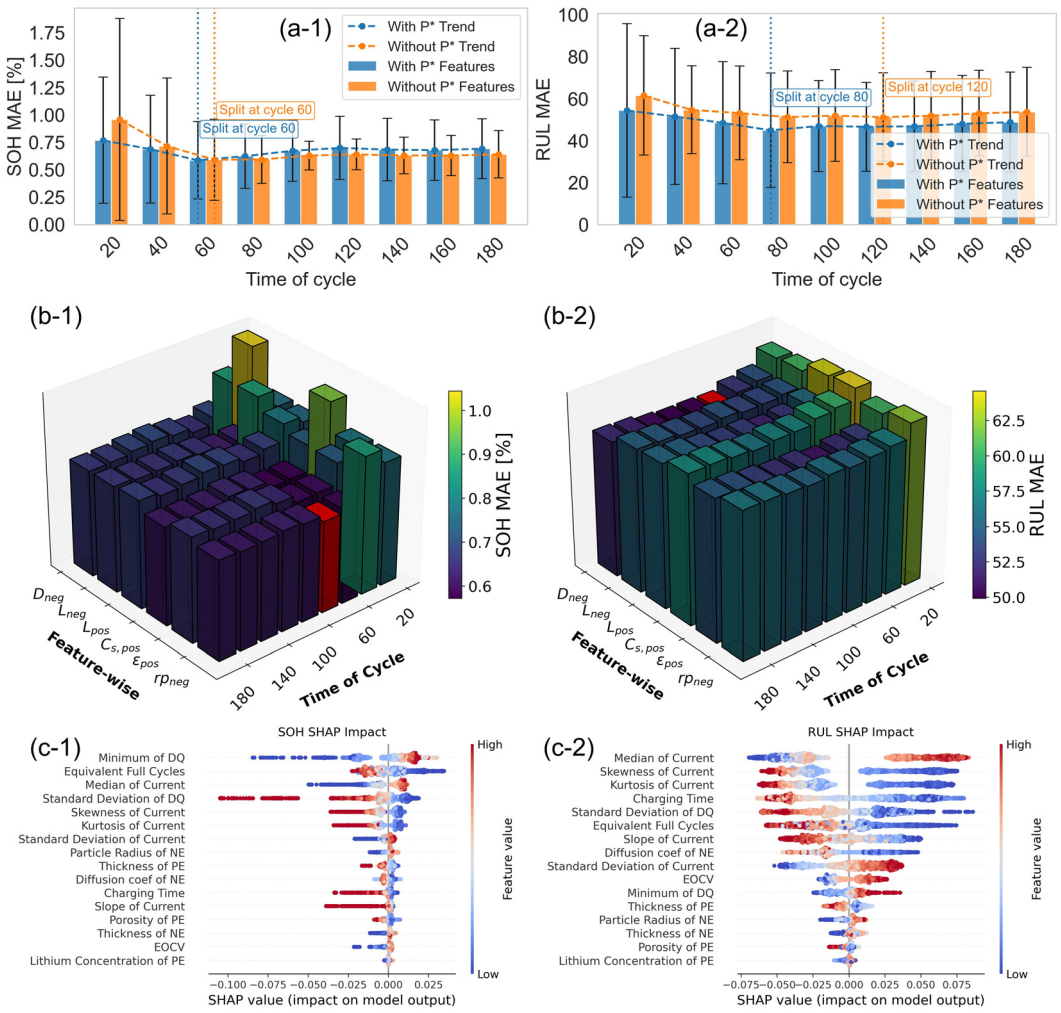

Fig. 5 Feature-wise and cycle-wise prediction performance. (a) Cycle-wise prediction error using a 16-dimensional feature vector, including six design features (P^*), to evaluate early-cycle model performance. (b) Early-cycle prediction error when including only one P^* feature alongside the other 15 manual features. The color gradient reflects the magnitude of error. Darker (purple) implies lower MAE (better performance), and brighter (yellow) indicates higher MAE. (c) SHAP analysis of the RF model showing feature importance for SOH estimation and RUL prediction in early cycles (at 6.7% and 8.4% of the median cycle life), based on the final outputs.

integrating design parameters enhances RUL prediction across all training ratios – most notably at higher data availability – by consistently improving accuracy and stability. All comparisons are based on the inclusion of all six P^* features, using the same hyperparameters as the baseline ML model (RF + MMD). Results demonstrate that P^* features enhance both SOH estimation and RUL prediction, with especially notable gains at 70–80% training ratios, thereby highlighting their practical value in uncertain deployment scenarios.

3.2. Performance including learned design parameters

The impact of design parameters (P^*) on prediction performance across fast charging protocols is further evaluated through feature and cycle-wise analyses. The model is trained on full-cycle data from a subset of cells (with a train ratio of 0.8), and evaluated using only early-cycle features (*e.g.* cycle 20 *vs.* cycle 180) from unseen test cells, simulating realistic deployment scenarios. As shown in Fig. 5, MAE is evaluated using optimized RF hyperparameters (see Table S5), comparing models with and without the inclusion of the six design parameters P^*. Based on their Spearman correlation coefficients (ρ) with SOH and RUL, these six features were prioritized over the remaining 10 manually engineered features (see Fig. S9) and forcibly included at the top of the selected feature pool. Fig. 5(a) analyzes the effect of P^* on early-stage SOH and RUL accuracy. In SOH estimation (Fig. 5(a-1)), the inclusion of P^* significantly reduces the MAE – dropping from 0.95% to 0.76% at cycle 20, a 20% improvement. The smaller error bars (MAE standard deviation) further indicate enhanced prediction stability. However, after cycle 60, the performance gap narrows, and the model without P^* slightly outperforms the one with P^* (0.59% *vs.* 0.62%), suggesting diminishing benefits of P^* in later stages. This can be explained by the fact that SOH estimation primarily depends on statistical patterns in voltage, current, and capacity. In the early stages of battery life, these patterns are subtle, and design parameters, such as the particle radius in the negative electrode, help capture underlying degradation signals. As aging progresses, usage-based features become more informative, reducing the added value of P^*. In RUL prediction (Fig. 5(a-2)), P^* integration consistently improves early-cycle performance. At cycle 20, the MAE decreases from 62 EFCs (without P^*) to 54 EFCs (with P^*), reflecting a 13% improvement. The overall trend with P^* is more stable and less sensitive to cycle variability. Although the MAE standard deviation is slightly higher with P^*, the model still maintains lower average error, even beyond 80 cycles, indicating stronger long-term predictive accuracy. The results confirm that RUL prediction benefits more from embedded physical knowledge. P^* features capture intrinsic aging behavior linked to design factors such as lithium diffusivity and electrode geometry – key drivers of long-term degradation – that manually engineered features alone cannot fully represent.

Since the P^* features collectively capture comprehensive degradation aspects, using data before the 80th cycle is sufficient for accurate prediction (see Fig. 5(a)). However, this result is based on incorporating all six P^* features. Fig. 5(b) further evaluates early-cycle prediction errors when each P^* is individually combined with 15 manual engineered features. For SOH estimation, $r_{p,neg}$ shows the lowest MAE across all cycles (except at cycle 40), reaching 0.7% MAE, and suggesting that it is the most effective standalone parameter for SOH estimation. The diffusion coefficient D_{neg} shows the highest MAEs, exceeding 1% in early cycles. From an electrochemical modelling perspective, the particle radius of negative electrode ($r_{p,neg}$) directly determines the specific area Av, denoted by $Av = 3\varepsilon_{neg}/r_{p,neg}$. This specific area influences the local current density associated with side reactions such as SEI growth, lithium plating, and particle cracking, making $r_{p,neg}$ highly relevant for SOH estimation. In contrast, D_{neg} directly affects lithium-ion transport kinetics and solid-state diffusion efficiency. While this factor does not directly alter capacity in the short term, it plays a critical role in long-term degradation, making it less sensitive for early SOH estimation. For RUL prediction, D_{neg} consistently produces the lowest RUL MAE across all cycles, around 50–54 EFCs, thereby outperforming all other parameters. However, $C_{s,pos}$ yield higher errors (up to 60EFCs), especially in early cycles, reflecting limited standalone usefulness for RUL prediction. For mechanistic interpretation, D_{neg} governs the solid-state diffusion of lithium ions within the negative electrode, a key factor for solid-state transport.[61] Under fast charging conditions, limited diffusion in the graphite electrode can trigger lithium plating,[62] making D_{neg} highly relevant for accurate RUL prediction under aggressive charging protocols.

A detailed cycle-wise comparison of the probability density distribution (PDD) of SOH and RUL prediction errors for each P^* feature is presented in Fig. S10 and S11. For SOH estimation, it can be observed that $r_{p,neg}$ shows consistently sharp and narrow error peaks across most cycles (from cycle 60 to 120), which implies a high robustness and accuracy. For RUL prediction, D_{neg} has a narrow and high peak near 10% error rate, indicating relatively stable early prediction performance. Other features (*i.e.*, $C_{s,pos}$, L_{pos}, $epss_{pos}$) show distributed tails, suggesting more uncertainty. The two KL divergence plots (see Fig. S12 and S13) offer insights into feature substitutability and task-specific sensitivity for both SOH estimation and RUL prediction. Combined with the above analysis, $r_{p,neg}$ is uniquely important for SOH estimation. It is not easily replaced by $epss_{pos}$, D_{neg}, or $C_{s,pos}$ (high KL), while L_{neg} and L_{pos} offer partial substitution. Solid-state diffusion coefficient D_{neg} is the most informative parameter for RUL prediction, especially in early cycle life, and not interchangeable with others. After cycle 100, $r_{p,neg}$ and L_{neg} become reasonable substitutes as KL divergence drops – implying that aging signals converge and different features encode similar aging behavior.

To further validate the sensitivity of the design parameters for different prediction tasks, we assess ML performance variations based on sequential removal of P^* features (see Fig. S14 and S15), following the order: $epss_{pos}$, L_{pos}, L_{neg}, D_{neg}, $C_{s,pos}$, and $r_{p,neg}$. The results show that adding P^* features markedly improves both SOH and RUL prediction accuracy. The most notable SOH gain occurs when $r_{p,neg}$ is retained alone, reinforcing its critical role in capacity-related degradation.

Importantly, this result suggests that the chosen set of features does not provide useful information regarding the capacity fade beyond what is already provided by $r_{p,neg}$. For RUL, the highest accuracy is achieved when four features, D_{neg}, $r_{p,neg}$, L_{neg}, and $C_{s,pos}$, are retained, highlighting D_{neg}'s primary influence and suggesting $r_{p,neg}$ and L_{neg} as effective substitutes. Fig. 5(c) provides the SHAP-based feature importance for SOH estimation at cycle 60 and RUL prediction at cycle 80, based on the final model outputs. To statistically quantify feature importance, the average absolute SHAP values over 10 different train-test splits are reported as a heatmap in Fig. S16. For SOH estimation, the most influential features are the minimum of ΔQ, EFCs, and median of current, as evidenced by their consistently high SHAP values across samples. This indicates that SOH is strongly influenced by usage history and charging variability. Among the design parameters, the particle radius of the negative electrode (NE) ($r_{p,neg}$), and thickness of positive electrode (PE) (L_{pos}) show moderate impact (SHAP values ± 0.02), suggesting their supplementary role in capturing the key aging mechanisms. In contrast, concentration of PE ($C_{s,pos}$) shows the lowest SHAP values, indicating minimal direct contribution to SOH estimation. Interestingly, the RUL SHAP impact plot (Fig. 5(c-2)) shows that embedded design knowledge plays a more prominent role: the diffusion coefficient in the NE (D_{neg}) stands out as the most influential physical features (SHAP impact up to ± 0.05), highlighting its importance in long-term mass transport and aging progression. The thickness of PE (L_{pos}) and particle radius of NE ($r_{p,neg}$) also contribute (SHAP up to ± 0.02), reinforcing the mechanistic relevance of electrode design parameters in aging prediction. Again, the limited influence of the porosity and lithium-ion concentration in the PE (ε_{pos} and $C_{s,pos}$) can be attributed to their indirect roles in fast-charging processes. While they modulate electrolyte accessibility and local concentration gradients—thereby influencing lithium-ion transport and reaction kinetics—they do not directly govern solid-state diffusion or interfacial reaction rates, which are primarily determined by the intrinsic properties of the active material.[63]

It is worth noting that SOH estimation depends more on statistical and usage-related features, with moderate contributions from material design factors such as particle radius in the NE. In contrast, RUL prediction depends substantially on design parameters, particularly the diffusion coefficient and architecture of both PE and NE. This contrast highlights the complementary roles of usage and design features in short-term *versus* long-term battery health prediction.

3.3. Performance comparison using different ML methods

To comprehensively evaluate the proposed ML pipeline and assess the impact of learned design parameters (P^*), we then aim to: (1) compare the performance of various ML models with and without the inclusion of P^*; and (2) analyze why integrating these parameters leads to improved predictive accuracy over models that exclude them. Linear regression from the Scikit-learn library is used as the baseline to benchmark the impact of incorporating P^* and comparing different ML models (see SI3). An 80 : 20 train-test split is applied, and all evaluations are repeated across 10 random splits to ensure consistency. As shown in Fig. 6(a), SOH and RUL prediction errors are compared across five ML models under three settings: (a) NoPhysParam_No P^*: models are trained without design parameters. (b) NoPhysParam_With P^*: design parameters are added, but the model uses the same hyperparameters from the no-P^* setting. (c) WithPhysParam_With P^*: design parameters are included, and new hyperparameters are re-optimized based on the updated feature set. For SOH estimation, the absence of P^* (NoPhysParam_No P^*) leads to the highest MAE with linear regression (0.083), indicating limited predictive capability. Incorporating P^* (NoPhysParam_With P^* and WithPhysParam_With P^*) on the other hand reduces the MAE to 0.050 (40% improvement). Advanced models like RF further lower the MAE to 0.020, representing a 76% reduction compared to the baseline. For RUL prediction, the baseline model without P^* yields an MAE above 130 EFCs. Adding P^* reduces the error to 88.45 EFCs (35% improvement), and integrating full design parameters with RF further lowers the MAE to 60.73 EFC (55% improvement). As detailed in Table 1, integrating design parameters reduces SOH MAE by up to 47% (*e.g.*, MLP: 0.064 → 0.034) and RUL MAE by up to 36% (*e.g.*, MLP: 160.15 → 103.19). The RF model thus achieves the best overall performance, with SOH MAE of 0.020, RUL MAE of 60.73 EFCs, and a training time of merely 1.09 s. When employing a lightweight model such as linear regression, integrating design parameters reduces SOH MAE by up to 40% and RUL MAE by up to 35%, with a training time of just 3 ms. Furthermore, the standard deviation consistently decreases after integrating design parameters, with SOH improving from 7% (RF) to 65% (MLP), and RUL from 56% (RF) to 69% (linear regression). These results confirm that incorporating P^* significantly enhances predictive accuracy with minimal computational cost.

To further illustrate the influence of the learned design parameters on SOH and RUL predictions, SHAP analysis is used to the RF model (Fig. S21). The most impactful features for SOH are usage-derived metrics, including the median of current, EFCs, and minimum of DQ. Among design parameters, the thickness of the PE and NE, along with the particle radius, show notable SHAP values, suggesting a potential link between thicker electrodes, larger particle size, and lower SOH. In contrast, RUL prediction depends on both usage metrics and multiple design parameters. Specifically, the diffusion coefficient and thickness of the negative electrode exhibit significant SHAP values, highlighting their strong influence on lifetime prediction. This can be explained by the fact that key physical properties—such as the diffusion coefficient within active particles and the charge transfer resistance (R_{ct}) at the electrode–electrolyte interfaces—are strongly linked to ion transport and are critical for enabling fast charging. Notably, L_{neg} is an input variable for calculating R_{ct}, expressed as: $R_{ct} = \frac{1}{L_{neg} A_v} \frac{RT}{j_{tot}(\alpha_a + \alpha_c)F}$. This mechanistic relationship supports why D_{neg} and L_{neg} consistently rank as highly important features for RUL prediction, especially under fast charging conditions.

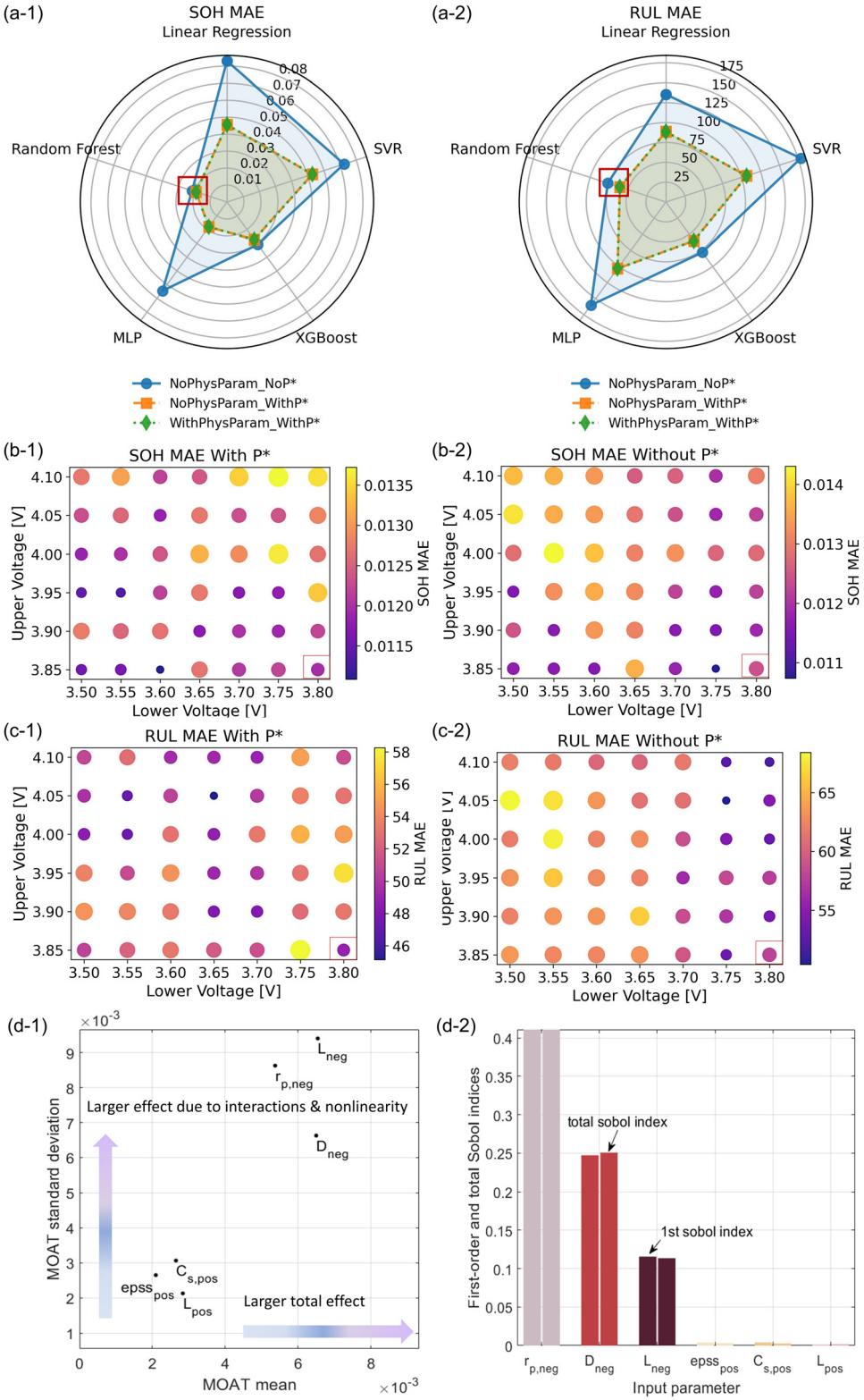

Fig. 6 Performance evaluations with and without integration of design features (*P**) across different applications. (a) Comparison of health status prediction accuracy across different ML models, with and without *P** inclusion. (b) and (c) Performance of the RF pipeline using partial charging curves across varying voltage windows, (b) SOH estimation and (c) RUL prediction. The color bar represents the corresponding performance metric, where brighter and larger bubbles indicate better results. (d) Sensitivity analysis of six *P** using a DT model, based on Morris one-at-a-time (MOAT) effects and Sobol indices.

Table 1 Test mean absolute errors (MAE) and computational cost for different ML models

			SOH		RUL		
Models	#Features	Physics parameters	MAE	STD	MAE	STD	Train time [s]
Linear regression	16^{m}	No	0.083	0.10	135.53	92.79	0.001
	$10^{m} + 6^{d}$	Yes	0.050	0.038	88.45	29.21	0.003
SVR	16^{m}	No	0.072	0.028	178.31	156.89	1.58
	$10^{m} + 6^{d}$	Yes	0.049	0.026	106.81	49.49	1.24
XGBoost	16^{m}	No	0.030	0.029	77.98	25.17	0.61
	$10^{m} + 6^{d}$	Yes	0.027	0.017	60.16	9.03	1.37
MLP	16^{m}	No	0.064	0.060	160.15	137.03	1.39
	$10^{m} + 6^{d}$	Yes	0.034	0.021	103.19	55.82	1.54
RF (this study)	16^{m}	No	0.023	0.014	76.76	18.53	1.11
	$10^{m} + 6^{d}$	Yes	0.020	0.008	60.73	8.10	1.09

m: manually engineered features. d: design parameters.

The robustness of the RF pipeline is further evaluated under different voltage ranges. These input voltage window conditions determine the available feature information. Results are presented in Fig. 6(b and c). With P^*, the prediction accuracy become less dependent on the input voltage window size. For SOH estimation, MAEs with P^* range mostly between 0.011 and 0.0135, showing tighter and more consistent accuracy. Over 50% of the voltage windows achieve MAE < 0.0125, including narrow segments such as [3.8 V, 3.85 V], thus demonstrating robustness also with limited data. Without P^*, MAEs are more dispersed (0.01 to 0.014), with fewer windows achieving low-error performance. For RUL prediction, RF model with P^* consistently achieve lower errors (45 to 58 EFCs) compared to those without P^* (55 to 65 EFCs), even in narrow windows [3.8 V, 3.85 V], indicating improved accuracy and stability. This is particularly important in real-world V2G applications, where bidirectional energy exchange between vehicles and charging stations is often limited to short-term or partial charging segments (typically $\sim$50% SOC), without access to full voltage cycles.[64] Fig. S22 shows that incorporating P^* leads to more stable and uniformly accurate SOH estimation, even though models without P^* occasionally achieve comparable peak performance. For RUL prediction, P^* offer a clear advantage, with over 75% of voltage windows achieving an R^2 greater than 0.91, demonstrating consistently high accuracy and robustness.

To interpret the physical meaning of these features, we conduct a sensitivity analysis using the DT model,[54] varying each design parameters to assess its contribution to predicted capacity variability. Based on sensitivity analysis, parameters such as the $r_{p,neg}$, D_{neg}, and L_{neg} and exhibit the most significant influence on battery capacity fade, as reflected in both Morris one-at-a-time (MOAT) and Sobol indices (Fig. 6(d)). These parameters play critical roles in governing lithium-ion transport within the negative electrode active material, influencing key factors such as active surface area,[65] diffusion rate,[66] and ion transport pathways.[67] Together, they shape the electrochemical kinetics of the cell, which directly affect the aging mechanisms. The kernel density estimation (KDE) plots offer further insight into how design parameters uncertainties translate into variations in predicted capacity (Fig. S23). Notably, $r_{p,neg}$, D_{neg} and L_{neg} produce broad, smooth distributions, indicating their high but stable influence. This is ideal for enhancing both SOH estimation stability and RUL trend prediction. In contrast, L_{pos} shows a multimodal distribution, suggesting nonlinear or regime-dependent effects, which may introduce variability during long-term aging modelling (RUL). Parameters like $C_{s,pos}$ and $epss_{pos}$ display weaker influence, pointing to their limited but potentially directional impact.[58,68]

4. Conclusions

In this work, we propose a framework for extracting six design parameters directly from random partial charging curves using DT simulation data. These parameters include solid-state diffusion coefficient, negative electrode thickness, positive electrode thickness, particle radius, lithium-ion concentration, and porosity. They exhibit strong predictive capability across various fast charging conditions and dynamic discharging. The key advantage over traditional feature engineering lies in the ability of this framework to capture hidden upstream design information encoded in fast charging protocols – without depending solely on predefined, manually crafted features. With this method, sensitive design parameters can be inferred within seconds, reducing SOH and RUL prediction variability by up to 65% and 69%, respectively. This integration achieves an SOH MAE of 0.020 and an RUL MAE of 60.73 EFCs in just 1 second, thereby outperforming the random forest model built on 16 manually engineered, physically interpretable features. This demonstrates that incorporating design parameters into the ML framework enables more stable and interpretable predictions while keeping a low computational cost. Notably, our findings reveal for the first time that SOH estimation is primarily driven by statistical and usage-based indicators, with particle radius in the negative electrode being the most influential parameter. In contrast, RUL prediction is more dependent on design parameters—especially those governing solid-state diffusion and electrode architecture. We believe that the

proposed framework enables seamless integration with upstream tasks and supports advanced BMS strategies across diverse electrification applications, including emerging scenarios such as V2G.

In the future, extending this framework to include electrolyte-related parameters, such as ionic conductivity, lithium transference number, and solvent composition, could further enhance its ability to capture aging mechanisms and guide cell design. This framework offers a practical tool for battery developers to efficiently identify how key design parameters evolve under specific conditions and to formulate targeted design strategies accordingly. From the end-user perspective, the physics-informed framework enables scenario-aware battery usage, helping to minimize degradation and enhance both lifetime and safety in EVs and stationary storage systems.

Conflicts of interest

There are no conflicts of interest to declare.

Data availability

Supplementary Figs. 1–23, Tables 1–6, notes, discussion and references. See DOI: **https://doi.org/10.1039/d5ee03268g**

The raw data generated in this study including aging data, RPT data, processed data, and data generated using a digital twin model are available at Zenodo, at **https://doi.org/10.5281/zenodo.16538328**. Code for the modeling work is deposited at **https://github.com/WendiGuo888/Uncovering_the_Impact_of_Battery_Design_Parameters.git**.

Acknowledgements

This work is supported by Nordic Energy Research (Vehicle battery storage for green transport and grid stability in the Nordics), the Swedish Electromobility Center and the Swedish Energy Agency project EV drivers in the driver's seat. We also acknowledge support from Batteries Sweden and the STandUP for Energy and COMPEL consortia.

References

1 B. Jiang, W. E. Gent, F. Mohr, S. Das, M. D. Berliner, M. Forsuelo, H. Zhao, P. M. Attia, A. Grover, P. K. Herring, M. Z. Bazant, S. J. Harris, S. Ermon, W. C. Chueh and R. D. Braatz, *Joule*, 2021, **5**, 3187–3203.
2 J. Yang, F. Gu and J. Guo, *Resour., Conserv. Recycl.*, 2020, **156**, 104713, DOI: **10.1016/j.resconrec.2020.104713**.
3 G. Ma, S. Xu, B. Jiang, C. Cheng, X. Yang, Y. Shen, T. Yang, Y. Huang, H. Ding and Y. Yuan, *Energy Environ. Sci.*, 2022, **15**, 4083–4094.
4 K. A. Severson, P. M. Attia, N. Jin, N. Perkins, B. Jiang, Z. Yang, M. H. Chen, M. Aykol, P. K. Herring, D. Fraggedakis, M. Z. Bazant, S. J. Harris, W. C. Chueh and R. D. Braatz, *Nat. Energy*, 2019, **4**, 383–391.
5 M. Dubarry, D. Howey and B. Wu, *Joule*, 2023, **7**, 1134–1144.
6 A. Mistry, S. Trask, A. Dunlop, G. Jeka, B. Polzin, P. P. Mukherjee and V. Srinivasan, *J. Electrochem. Soc.*, 2021, **168**, 070536.
7 A. Geslin, L. Xu, D. Ganapathi, K. Moy, W. C. Chueh and S. Onori, *Nat. Energy*, 2025, **10**, 172–180, DOI: **10.1038/s41560-024-01675-8**.
8 X. G. Yang, Y. Leng, G. Zhang, S. Ge and C. Y. Wang, *J. Power Sources*, 2017, **360**, 28–40.
9 R. Li, N. D. Kirkaldy, F. F. Oehler, M. Marinescu, G. J. Offer and S. E. J. O'Kane, *Nat. Commun.*, 2025, **16**, 2776, DOI: **10.1038/s41467-025-57968-3**.
10 W. Guo, Y. Li, Z. Sun, S. B. Vilsen and D. I. Stroe, *Energy Storage Mater.*, 2023, **63**, 102965.
11 A. Weng, P. Mohtat, P. M. Attia, V. Sulzer, S. Lee, G. Less and A. Stefanopoulou, *Joule*, 2021, **5**, 2971–2992.
12 J. Rhyu, J. Schaeffer, M. L. Li, X. Cui, W. C. Chueh, M. Z. Bazant and R. D. Braatz, *Joule*, 2025, 101884.
13 M. Alipour, S. S. Tavallaey, A. M. Andersson and D. Brandell, *ChemPhysChem*, 2022, **23**, e202100829, DOI: **10.1002/cphc.202100829**.
14 M. Aykol, C. B. Gopal, A. Anapolsky, P. K. Herring, B. van Vlijmen, M. D. Berliner, M. Z. Bazant, R. D. Braatz, W. C. Chueh and B. D. Storey, *J. Electrochem. Soc.*, 2021, **168**, 30525.
15 W. Guo, Z. Sun, S. B. Vilsen, J. Meng and D. I. Stroe, *J. Energy Storage*, 2022, **56**, 105992.
16 M. Alipour, L. Yin, S. S. Tavallaey, A. M. Andersson and D. Brandell, *J. Power Sources*, 2023, **579**, 233273, DOI: **10.1016/j.jpowsour.2023.233273**.
17 S. Tao, M. Zhang, Z. Zhao, H. Li, R. Ma, Y. Che, X. Sun, L. Su, C. Sun, X. Chen, H. Chang, S. Zhou, Z. Li, H. Lin, Y. Liu, W. Yu, Z. Xu, H. Hao, S. Moura, X. Zhang, Y. Li, X. Hu and G. Zhou, *Energy Environ. Sci.*, 2025, **18**, 1544–1559, DOI: **10.1039/d4ee03839h**.
18 J. Huang, S. T. Boles and J. M. Tarascon, *Nat. Sustainability*, 2022, **5**, 194–204, DOI: **10.1038/s41893-022-00859-y**.
19 C. W. Hsu, R. Xiong, N. Y. Chen, J. Li and N. T. Tsou, *Appl. Energy*, 2022, **306**, 118134, DOI: **10.1016/j.apenergy.2021.118134**.
20 V. Steininger, K. Rumpf, P. Hüsson, W. Li and D. U. Sauer, *Cell Rep. Phys. Sci.*, 2023, **4**, 101596, DOI: **10.1016/j.xcrp.2023.101596**.
21 S. Kim, Z. Yi, M. R. Kunz, E. J. Dufek, T. R. Tanim, B. R. Chen and K. L. Gering, *Cell Rep. Phys. Sci.*, 2022, **3**, 101023, DOI: **10.1016/j.xcrp.2022.101023**.
22 M. Kim, I. Kim, J. Kim and J. W. Choi, *ACS Energy Lett.*, 2023, **8**, 2946–2953.
23 F. Wang, Z. Zhai, Z. Zhao, Y. Di and X. Chen, *Nat. Commun.*, 2024, **15**, 4332, DOI: **10.1038/s41467-024-48779-z**.
24 S. Tao, C. Sun, S. Fu, Y. Wang, R. Ma, Z. Han, Y. Sun, Y. Li, G. Wei, X. Zhang, G. Zhou and H. Sun, *ACS Energy Lett.*, 2023, **8**, 3269–3279.
25 Y. Zhang, Q. Tang, Y. Zhang, J. Wang, U. Stimming and A. A. Lee, *Nat. Commun.*, 2020, **11**, 1706, DOI: **10.1038/s41467-020-15235-7**.

26 I. Bloom, A. N. Jansen, D. P. Abraham, J. Knuth, S. A. Jones, V. S. Battaglia and G. L. Henriksen, *J. Power Sources*, 2005, **139**, 295–303.
27 A. Weng, J. B. Siegel and A. Stefanopoulou, *Front. Energy Res.*, 2023, **11**, DOI: 10.3389/fenrg.2023.1087269.
28 M. Dubarry, C. Truchot and B. Y. Liaw, *J. Power Sources*, 2012, **219**, 204–216.
29 P. Gasper, A. Schiek, K. Smith, Y. Shimonishi and S. Yoshida, *Cell Rep. Phys. Sci.*, 2022, **3**, 101184, DOI: 10.1016/j.xcrp.2022.101184.
30 J. Schaeffer, P. Gasper, E. Garcia-Tamayo, R. Gasper, M. Adachi, J. Pablo Gaviria-Cardona, S. Montoya-Bedoya, A. Bhutani, A. Schiek, R. Goodall, R. Findeisen, R. D. Braatz and S. Engelke, *J. Electrochem. Soc.*, 2023, **170**, 060512.
31 D. Yang, X. Zhang, R. Pan, Y. Wang and Z. Chen, *J. Power Sources*, 2018, **384**, 387–395.
32 Y. Che, Y. Zheng, Y. Wu, X. Sui, P. Bharadwaj, D. I. Stroe, Y. Yang, X. Hu and R. Teodorescu, *Appl. Energy*, 2022, **323**, 119663, DOI: 10.1016/j.apenergy.2022.119663.
33 S. C. Yang, Y. Hua, D. Qiao, Y. B. Lian, Y. W. Pan and Y. L. He, *Electrochim. Acta*, 2019, **326**, 134928, DOI: 10.1016/j.electacta.2019.134928.
34 C. Yuan, Y. Hahn, W. Lu, V. Oancea and J. Xu, *Cell Rep. Phys. Sci.*, 2022, **3**, 101158.
35 X. Duan, B. Li, J. Li, X. Gao, L. Wang and J. Xu, *Adv. Energy Mater.*, 2023, **13**, 2203767, DOI: 10.1002/aenm.202203767.
36 X. Duan, J. Li, Y. Jia, X. Gao, L. Wang and J. Xu, *Adv. Sci.*, 2023, **10**, 2302496, DOI: 10.1002/advs.202302496.
37 X. Hu, L. Xu, X. Lin and M. Pecht, *Cell Press*, 2020, **4**, 310–346, DOI: 10.1016/j.joule.2019.11.018.
38 C. R. Birkl, M. R. Roberts, E. McTurk, P. G. Bruce and D. A. Howey, *J. Power Sources*, 2017, **341**, 373–386.
39 M. Gaberšček, *Nat. Commun.*, 2021, **12**, 19–22.
40 C. Bommier, W. Chang, Y. Lu, J. Yeung, G. Davies, R. Mohr, M. Williams and D. Steingart, *Cell Rep. Phys. Sci.*, 2020, **1**, 100035, DOI: 10.1016/j.xcrp.2020.100035.
41 P. Pietsch and V. Wood, *Annu. Rev. Mater. Res.*, 2017, **47**, 451–479, DOI: 10.1146/annurev-matsci-070616.
42 P. Verma, P. Maire and P. Novák, *Electrochim. Acta*, 2010, **55**, 6332–6341.
43 A. M. Boyce, E. Martínez-Pañeda, A. Wade, Y. S. Zhang, J. J. Bailey, T. M. M. Heenan, D. J. L. Brett and P. R. Shearing, *J. Power Sources*, 2022, **526**, 231119, DOI: 10.1016/j.jpowsour.2022.231119.
44 Y. Bi, J. Tao, Y. Wu, L. Li, Y. Xu, E. Hu, B. Wu, J. Hu, C. Wang, J.-G. Zhang, Y. Qi and J. Xiao, *Science*, 2020, **370**, 1313–1317, DOI: 10.1126/science.abc3167.
45 H. Ruan, J. Chen, W. Ai and B. Wu, *Energy AI*, 2022, **9**, 100158, DOI: 10.1016/j.egyai.2022.100158.
46 Y. Zhang, T. Wik, J. Bergström and C. Zou, *Energy Storage Mater.*, 2025, **74**, 103877, DOI: 10.1016/j.ensm.2024.103877.
47 M. Dubarry, M. Berecibar, A. Devie, D. Anseán, N. Omar and I. Villarreal, *J. Power Sources*, 2017, **360**, 59–69.
48 S. Kim, Z. Yi, B. R. Chen, T. R. Tanim and E. J. Dufek, *Energy Storage Mater.*, 2022, **45**, 1002–1011.
49 P. R. Chinnam, A. M. Colclasure, B. R. Chen, T. R. Tanim, E. J. Dufek, K. Smith, M. C. Evans, A. R. Dunlop, S. E. Trask, B. J. Polzin and A. N. Jansen, *ACS Appl. Energy Mater.*, 2021, **4**, 9133–9143.
50 B. Chen, M. Cody, S. Kim, M. Ross, T. R. Tanim, J. Eric and E. J. Dufek, pp. 1–18.
51 J. Zhang, J. Qiao, K. Sun and Z. Wang, *Particuology*, 2022, **61**, 18–29, DOI: 10.1016/j.partic.2021.05.006.
52 P. Bai, J. Li, F. R. Brushett and M. Z. Bazant, *Energy Environ. Sci.*, 2016, **9**, 3221–3229.
53 A. M. Colclasure, T. R. Tanim, A. N. Jansen, S. E. Trask, A. R. Dunlop, B. J. Polzin, I. Bloom, D. Robertson, L. R. Flores, M. Evans, E. J. Dufek and K. Smith, *Electrochim. Acta*, 2020, **337**, 135854, DOI: 10.1016/j.electacta.2020.135854.
54 W. Guo, Z. Sun, J. Guo, Y. Li, S. B. Vilsen and D. I. Stroe, *Adv. Energy Mater.*, 2024, **14**, 2401644.
55 B. van Vlijmen, V. N. Lam, P. A. Asinger, X. Cui, J. Schaeffer, A. Geslin, D. Ganapathi, S. Sun, P. K. Herring, C. Balaji Gopal, N. Geise, H. D. Deng, H. L. Thaman, S. D. Kang, S. B. Torrisi, A. Trewartha, A. Anapolsky, B. D. Storey, W. E. Gent, R. D. Braatz and W. C. Chueh, *Energy Environ. Sci.*, 2025, **18**, 6641–6654, DOI: 10.1039/D4EE05609D.
56 W. Li, I. Demir, D. Cao, D. Jöst, F. Ringbeck, M. Junker and D. U. Sauer, *Energy Storage Mater.*, 2022, **44**, 557–570.
57 M. Song and S. Y. Choe, *Appl. Energy*, 2022, **305**, 117920.
58 Y. Li, J. Guo, K. Pedersen, L. Gurevich and D.-I. Stroe, *J. Energy Chem.*, 2023, **80**, 237–246, DOI: 10.1016/j.jechem.2023.01.016.
59 W. Guo, Z. Sun, Y. Li, S. Jin, S. B. Vilsen and D. I. Stroe, *IEEE*, 2024, 1673–1679, DOI: 10.1109/IPEMC-ECCEAsia60879.2024.10567562.
60 Y. Che, S. B. Vilsen, J. Meng, X. Sui and R. Teodorescu, *eTransportation*, 2023, **17**, 100245, DOI: 10.1016/j.etran.2023.100245.
61 Y. Huang, T. Wik, D. Finegan, Y. Li and C. Zou, *ChemRxiv*, 2025, preprint, DOI: 10.26434/chemrxiv-2025-qrkpq.
62 X. Lu, M. Lagnoni, A. Bertei, S. Das, R. E. Owen, Q. Li, K. O'Regan, A. Wade, D. P. Finegan, E. Kendrick, M. Z. Bazant, D. J. L. Brett and P. R. Shearing, *Nat. Commun.*, 2023, **14**, 5127, DOI: 10.1038/s41467-023-40574-6.
63 M. Weiss, R. Ruess, J. Kasnatscheew, Y. Levartovsky, N. R. Levy, P. Minnmann, L. Stolz, T. Waldmann, M. Wohlfahrt-Mehrens, D. Aurbach, M. Winter, Y. Ein-Eli and J. Janek, *Adv. Energy Mater.*, 2021, **11**, 2101126, DOI: 10.1002/aenm.202101126.
64 T. Lehtola, *Renewable Sustainable Energy Rev.*, 2025, **208**, 115013, DOI: 10.1016/j.rser.2024.115013.
65 R. Zhao, J. Liu and J. Gu, *Appl. Energy*, 2015, **139** 220–229.
66 Y. C. Chien, H. Liu, A. S. Menon, W. R. Brant, D. Brandell and M. J. Lacey, *Nat. Commun.*, 2023, **14**, 2289, DOI: 10.1038/s41467-023-37989-6.
67 G. Wang, A. Mijailovic, J. Yang, J. Xiong, S. E. Beasley, K. Mathew, B. Zhou, W. Lu, B. W. Sheldon and Q. Wu, *J. Mater. Chem. A*, 2023, **11**, 21793–21805.
68 Y. Huang, T. Wik, D. Finegan, Y. Li and C. Zou, *ChemRxiv*, 2025, preprint, DOI: 10.26434/chemrxiv-2025-qrkpq.

